Geophysical Research Letters

RESEARCH LETTER
10.1029/2023GL106992

Key Points:

- Coseismic ground deformation of the 2023 Morocco earthquake measured with interferometric synthetic aperture radar (InSAR) data
- InSAR data allow for two possibilities: the rupture of an intramontane high-angle fault or of a border low-angle thrust
- Based on aftershock distribution, crustal thickness, and regional tectonic stress orientation, the low-angle solution is more likely

Supporting Information:

Supporting Information may be found in the online version of this article.

Correspondence to:

D. Cheloni,
daniele.cheloni@ingv.it

Citation:

Cheloni, D., Famiglietti, N. A., Tolomei, C., Caputo, R., & Vicari, A. (2024). The 8 September 2023, M_W 6.8, Morocco earthquake: A deep transpressive faulting along the active high Atlas mountain belt. *Geophysical Research Letters*, *51*, e2023GL106992. https://doi.org/10.1029/2023GL106992

Received 27 OCT 2023
Accepted 26 DEC 2023

Author Contributions:

Conceptualization: D. Cheloni
Data curation: N. A. Famiglietti, C. Tolomei, A. Vicari
Formal analysis: D. Cheloni, N. A. Famiglietti, C. Tolomei, R. Caputo, A. Vicari
Investigation: D. Cheloni, R. Caputo
Methodology: D. Cheloni
Software: N. A. Famiglietti, C. Tolomei
Validation: D. Cheloni, N. A. Famiglietti, C. Tolomei, R. Caputo, A. Vicari
Visualization: D. Cheloni

The 8 September 2023, M_W 6.8, Morocco Earthquake: A Deep Transpressive Faulting Along the Active High Atlas Mountain Belt

D. Cheloni[1], N. A. Famiglietti[2], C. Tolomei[1], R. Caputo[3], and A. Vicari[2]

[1]Istituto Nazionale di Geofisica e Vulcanologia, Roma, Italy, [2]Istituto Nazionale di Geofisica e Vulcanologia, Sezione Irpina, Grottaminarda, Italy, [3]Department of Physics & Earth Sciences, Ferrara University, Ferrara, Italy

Abstract On 8 September 2023 an M_W 6.8 earthquake struck the High Atlas Mountains of western Morocco, about 70 km southwest from Marrakesh, causing significant devastation and casualties. In this study, we investigate a comprehensive geodetic data set, employing interferometric synthetic aperture radar measurements to assess the fault segment responsible for the seismic event. Our findings suggest two potential fault scenarios: either a transpressive NNW-dipping high-angle (70°) fault related to the Tizi n'Test alignment or a transpressive SSW-dipping low-angle (22°) fault associated with the North Atlas Fault, with slip (up to 2.2 m) only occurring on deeper parts of the fault. While seismic catalogs couldn't definitively determine the dip direction of the fault, evidence from mainshock locations, gravity and heat flow data and modeling, and active shortening direction suggest the activation of a low-angle south-westerly dipping oblique thrust of the North Atlas fault during the 2023 Moroccan earthquake.

Plain Language Summary On 8 September 2023, a powerful earthquake with a magnitude of 6.8 hit the High Atlas Mountains in western Morocco, causing significant damage and loss of life. In this research, a thorough geodetic analysis was conducted using a technique called interferometric synthetic aperture radar to identify the causative fault. The results suggest two potential fault scenarios: one involves a steeply dipping fault related to the Tizi n'Test crustal structure, while the other suggests a gently dipping fault associated with the North Atlas Fault. As far as existing aftershock records do not allow determination of the angle of the fault, clues from the locations of the mainshock, gravity and heat flow data and modeling, and the direction of active compression suggest that a gently dipping fault was likely activated during the 2023 earthquake in Morocco.

1. Introduction

The 2023 Morocco earthquake sequence started on 8 September 2023 at 11:11 p.m., local time, with a M_W 6.8 event, followed by a magnitude 4.9 aftershock 19 min later, striking the western sector of the High Atlas Mountains in Morocco (Figure 1), characterized by low geodetic strain rates (Koulali et al., 2011; Serpelloni et al., 2007). According to the Centre Sismologique Euro-Méditerranéen (CSEM), to the Portuguese Institute for Sea and Atmosphere (IPMA) and to the United States Geological Survey (USGS), the earthquake's hypocenter was located at a depth of about 20–25 km with its epicenter in the High Atlas Mountains, 70 km southwest of the city of Marrakesh. The earthquake was felt as far away as Portugal and Algeria. According to Morocco's Interior Ministry, at least 2,901 people were killed, mostly in Marrakech and in five provinces near the epicenter, and about 320,000 people were exposed to the earthquake, with the remote villages located in the High Atlas Mountains suffering substantial losses and extensive damage. The following seismic sequence was characterized by numerous aftershocks almost entirely shallower than the mainshock and located either in a cluster SSE of the mainshock (CSEM database), or mainly NNE of the epicenter (IPMA database) within the hanging-wall of the mainshock (bottom inset in Figure 1). Fault plane solutions for the main event exhibit transpressional faulting (U.S. Geological Survey, 2023), consistent with the direction of active shortening of about 1.0 ± 0.6 mm/yr in this sector of the High Atlas belt (Koulali et al., 2011). Previous geological studies (e.g., Bernard et al., 2010; Sebrier et al., 2006) have identifies several SW-NE trending compressive and transpressive fault systems, some of which were considered active in this area, often representing structures inherited from the Triassic extensional tectonic phases. However, the strain partitioning between the different fault systems and the recognition of the actual active fault segments is still not completely clear.

Writing – original draft: D. Cheloni, N. A. Famiglietti, C. Tolomei, R. Caputo, A. Vicari

Here we exploit a large data set of Interferometric Synthetic Aperture Radar (InSAR) measurements (Sentinel-1 and ALOS-2 satellites) to investigate the ground displacement field and to constrain, by using elastic dislocation modeling, the source parameters and slip distribution of the causative fault segment associated with the mainshock of the sequence. To examine our results, we also exploit the information of the aftershocks distribution and the known geologic structures of the area. Finally, we investigate the static Coulomb stress changes induced by the mainshock by examining both the contribution to the observed aftershock triggering during the 2023 Morocco sequence and to the adjacent fault segments loading.

2. Seismotectonic Settings and Seismicity

Morocco is located at the boundary between the African and the Eurasian plates. The oblique convergent motion of the African plate toward Eurasian plate is thus one of the primary drivers of the seismic activity in Morocco, with most of the seismicity localized in northernmost Morocco, in the Rif and Alboran Sea (Figure 1), where plate convergence trends roughly NW-SE with a rate of motion of about 4 mm/yr (e.g., Calais et al., 2003; Koulali et al., 2011; McClusky et al., 2003; Nocquet, 2003; Serpelloni et al., 2007). To the south, the mountainous Atlas region is characterized by moderate seismic activity, with clusters of scarce to moderate seismicity along the Middle and High Atlas mountain belts (Figure 1), representing the southernmost zone of the Eurasia-Africa collision zone.

Few damaging earthquakes have occurred in Morocco in the last century: the M_W 6.1–6.5 Al Hoceima 1994, 2014, and 2016 earthquakes in the Rif and Alboran Sea region, and the M_W 5.8 Agadir 1960 event located around the boundary between the western High Atlas and the Anti Atlas, respectively (Figure 1). The 8 September 2023, M_W 6.8, earthquake thus represents the strongest instrumentally recorded event in Morocco and the deadliest since the 1960 Agadir earthquake. The last earthquake of comparable size ($M > 6.5$) in Morocco was probably on 11 May 1624 near Fez, located somewhere along the main frontal thrust of the Rif in northern Morocco (Cherkaoui et al., 2017) (Figure 1). The few reliable focal mechanisms available on the Atlas seismicity indicate a general present-day compressional regime with average NNW-trending P axes (Medina & Cherkaoui, 1991), in agreement with an oblique convergence characterized by transpressive deformations. Actual GPS data confirm that deformation along the High Atlas is still active, accommodating about 1.0 ± 0.6 mm/yr WNW-ESE oriented shortening (Koulali et al., 2011).

Localization uncertainties however do not allow these seismic events to be associated with specific active fault zones, with seismic activity distributed in the Atlas region on a system of thrust and strike-slip faults. The major fault zones in the 2023 epicentral area are represented by the North and South Atlas border thrusts (North Atlas Fault [NAF] and South Atlas Fault [SAF]) (Sebrier et al., 2006) and by the steeply dipping transpressional Tizi n'Test Fault (TTF), located in the axial zone of the belt, which some authors consider no longer tectonically active (e.g., Sebrier et al., 2006), while others suggest evidence to thrust reactivation (Bernard et al., 2010, 2011; Ouayah et al., 2021).

3. Geodetic Data (Sentinel-1 and ALOS-2 InSAR Data)

We used InSAR data acquired by different satellites (Table S1 in Supporting Information S1) to retrieve the full coseismic displacement field. In particular, we exploited two ascending and two descending interferograms, which involve the Sentinel-1 (C-band) and the ALOS-2 (L-band) sensors, to measure the ground displacement related to the 8 September 2023, M_W 6.8, earthquake (Figure S1 in Supporting Information S1). The availability of interferograms from different sensors and several incidence angles allowed to retrieve the full coseismic displacement field, hence to better constraint the source modeling of the causative fault as well. All interferograms were processed using the classical two-steps SAR interferometry implemented in the SARscape® software included in the ENVI package. To assess the influence of topography during the InSAR processing we employed a Digital Elevation Model (DEM) with a spatial resolution of 30 m from the ALOS World 3D catalog (Takaku et al., 2014). To suppress noise, the multi-look ratio of the interferogram was set to 3:6 (range × azimuth direction) and 3 × 1 for the ALOS-2 and Sentinel-1 data, respectively, resulting in a 20 m final pixel dimension at ground. The formed interferograms were then filtered using the Goldstein method (Goldstein & Werner, 1998) to improve the signal-to-noise ratio of the result. Then, the phase was unwrapped adopting the minimum-cost flow algorithm (Costantini, 1998). Finally, the unwrapped phase was geocoded using the DEM in the UTM WGS84 reference system.

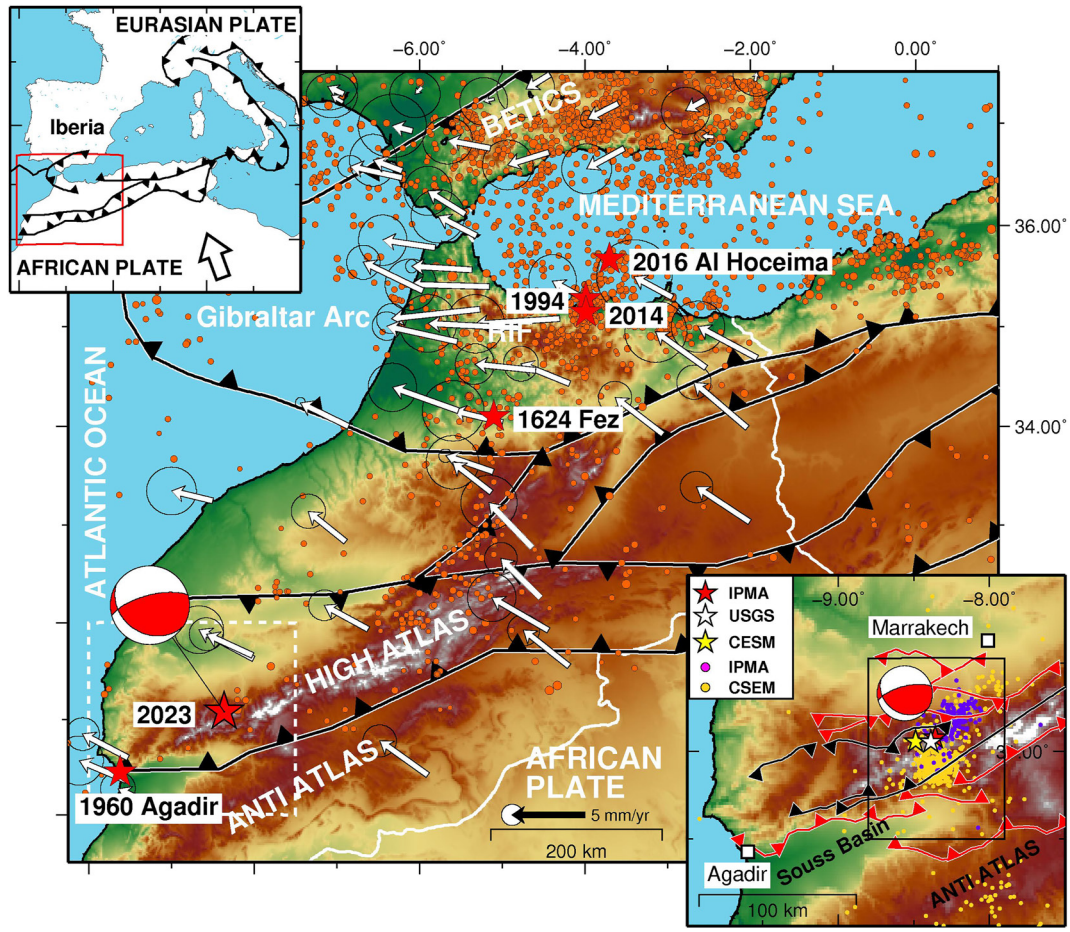

Figure 1. Seismotectonic framework of the study area. Solid barbed lines are major tectonic lineaments of the area. Seismicity: orange dots are instrumental earthquakes from the ESHM20 unified Euro-Mediterranean catalog (Grunthal & Whalstrom, 2012; Rovida & Antonucci, 2021); red stars represent the largest shocks ($M > 6$), including the 8 September 2023, M_W 6.8, mainshock. The white arrows represent the GPS velocity field of Koulali et al. (2011), showing the Africa plate motion relative to Eurasia. The upper inset shows a tectonic sketch of the western Mediterranean region, with the red box indicating the area of the main figure. The bottom inset is a sketch map of the active faults (modified from Sebrier et al. (2006)) and of the 2023 Morocco seismic sequence. Magenta (Institute for Sea and Atmosphere, available at https://www.ipma.pt/en/geofisica/sismicidade) and yellow (Centre Sismologique Euro-Méditerranéen, available at https://www.emsc-csem.org/) circles are the aftershocks of the first month after the mainshock. The box is the area of Figure 3.

The ground deformation retrieved from the four unwrapped interferograms (Figures 2 and 3) is characterized by a WSW-ENE striking deformation lobe located in the axial part of this sector of the High Atlas Mountains, between the TTF alignment to the south and the NAF border thrust to the north, with a maximum Line-Of-Sight (LOS) displacement of about 20 cm around the epicenter (positive LOS values represent decreasing distances from the satellite). The observed deformation captured by the InSAR images (Figure 2) suggests that the rupture was blind and consistent with either the planes derived from the focal mechanisms of the mainshock, allowing therefore the possibility of both the rupture of a steep NNW-dipping or of a gentle SSW-dipping fault, respectively. The distribution of the interferometric fringes (Figure S1 in Supporting Information S1) seems to suggest the high-angle fault. Displacement outcomes from the ascending and descending interferograms were also decomposed to estimate displacement motion for the E-W and vertical directions (Fialko and Simons, 2001) (Figure S2 in Supporting Information S1).

4. Geodetic Modeling

In this section, we illustrate the results of the geodetic source inversion on two different fault orientations corresponding to (a) a steep NNW-dipping fault scenario and to (b) a gentle SSW-dipping fault scenario, that is,

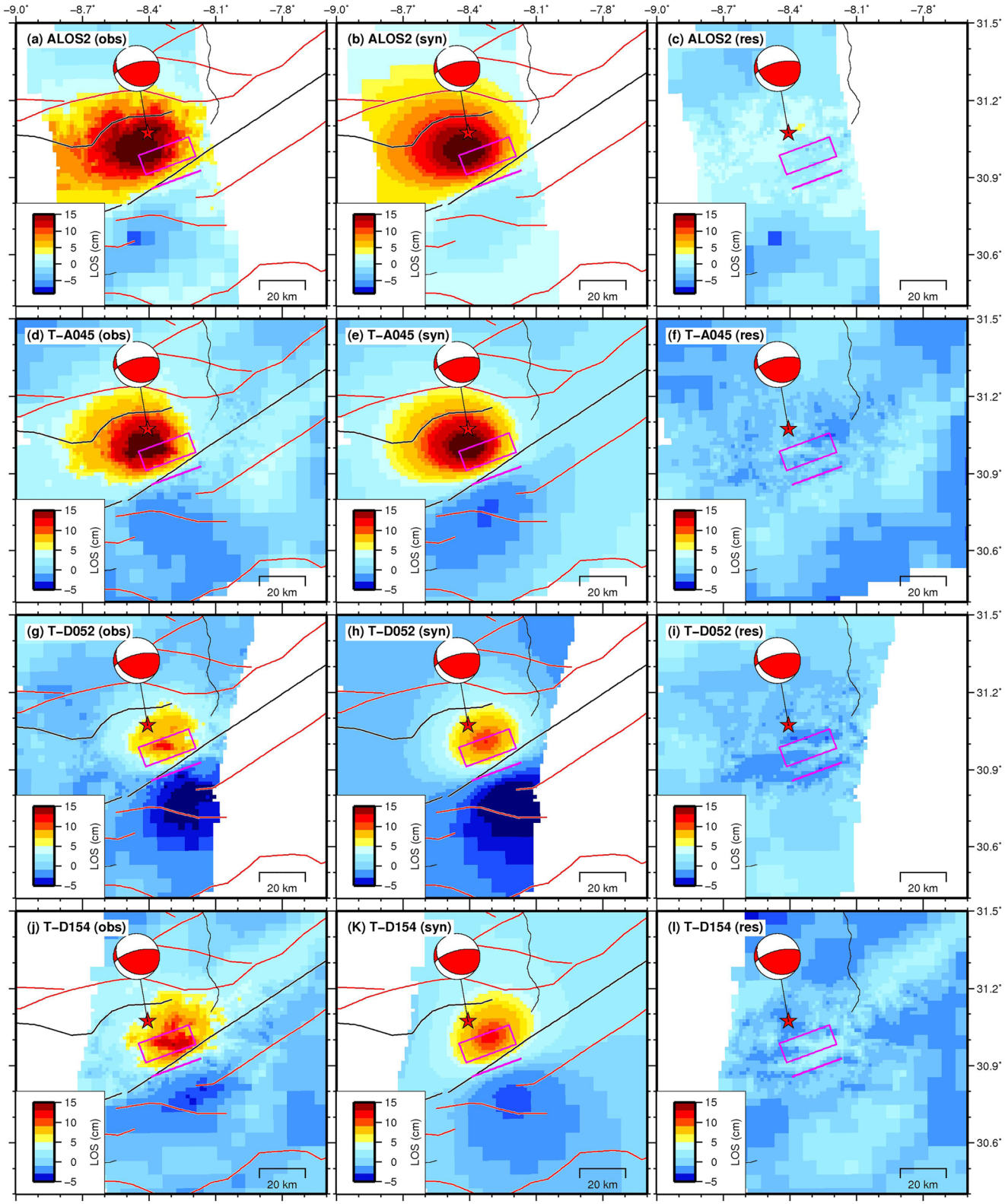

Figure 2. Displacement maps of the 8 September 2023, M_W 6.8, Morocco earthquake. Observed (left panels), modeled (middle panels), and residuals (right panels) interferometric synthetic aperture radar ALOS-2 ascending and Sentinel-1 ascending and descending unwrapped interferograms based on the high-angle NNW-dipping fault scenario. The red star is the mainshock provided by Institute for Sea and Atmosphere with its focal mechanism. Solid lines are the major fault of the area (modified from Sebrier et al. (2006)).

10.1029/2023GL106992

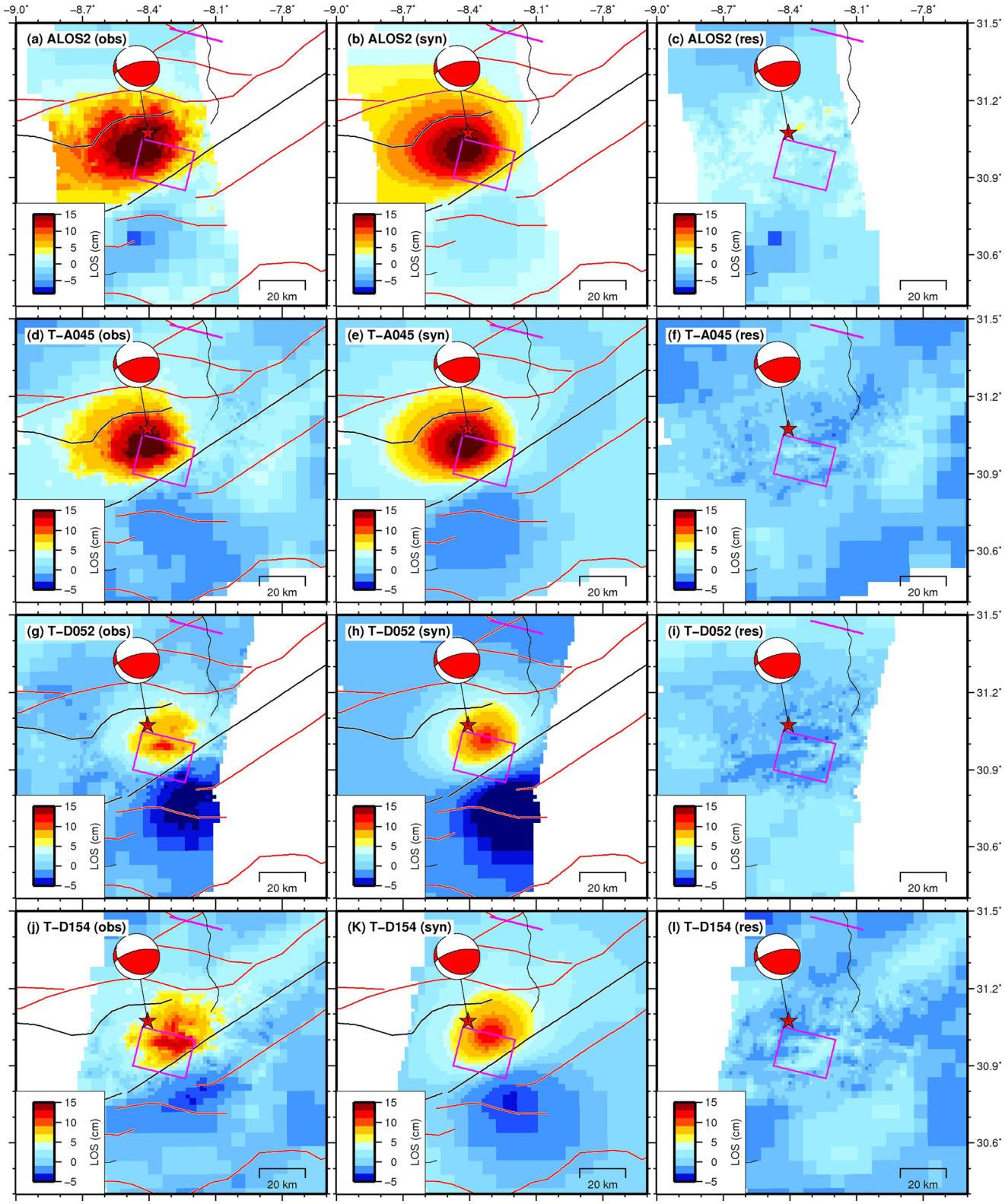

Figure 3. Displacement maps of the 8 September 2023, M_W 6.8, Morocco earthquake. Observed (left panels), modeled (middle panels), and residuals (right panels) interferometric synthetic aperture radar ALOS-2 ascending and Sentinel-1 ascending and descending unwrapped interferograms based on the low-angle SSW-dipping fault scenario. Symbols as in Figure 2.

testing either the planes as deduced from the focal mechanism solution, and we discuss to what extent which scenario is required by the data. We performed the geodetic modeling using rectangular dislocations in an elastic, homogeneous, and isotropic half-space (Okada, 1985), following a standard two-steps procedure (e.g., Atzori et al., 2009; Cheloni & Akinci, 2020; Cheloni et al., 2010): (a) we inverted the LOS displacements to retrieve the fault geometry independently from the seismological solutions and then (b) the best-fit uniform-slip solution is used as a priori for the estimation of the coseismic slip distribution. Before modeling, the InSAR displacement maps were down-sampled using a resolution-based down-sampling scheme (Lohman & Simons, 2005). We also apply positivity constraints and regularize the linear inversion by applying spatial smoothing (using the Laplacian operator, Figure S3 in Supporting Information S1). Additional terms consisting of a linear ramp for each InSAR interferogram are also included in the inversion.

4.1. Steep NNW-Dipping Fault Scenario

In the first step, we carried out a non-linear inversion of the fault geometry by using a simulated annealing algorithm (Corana et al., 1987). The best-fitting uniform-slip model is described by a 250° WSW-ENE striking and 69° NNW-dipping transpressive (rake about 60°) fault (18 × 22 km) plane, in good agreement with the steep dipping plane of the focal solution and with the preliminary USGS finite-fault model (strike/dip/rake 251°/69°/69°) (U.S. Geological Survey, 2023). The average uniform slip is 1.3 m, which using a value of 30 GPa for rigidity, yields an estimated seismic moment of 2.3×10^{19} Nm, equivalent to a M_W 6.8 earthquake. The fault top of our model is quite consistent with the surficial trace of the TTF (Figure 4a).

In the second step, we extended the uniform-slip fault to capture the area affected by aftershocks and subdivided the fault into small patches of constant size, solving for slip magnitude on each patch, while fixing the rake to the best fit value of the uniform-slip solution. The best-fitting slip distribution on the extended fault plane (50 × 50 km) is shown in Figure 4a. The data are well reproduced (Figure 2) but the fit to the data does not improve significantly passing from the uniform-slip to a variable slip model (Table S2 in Supporting Information S1). The coseismic slip distribution model shows a major asperity with peak slip of about 2.2 m, located down-dip respect to the hypocenter and roughly contained in the uniform-slip fault, leaving therefore unbroken the upper part of the fault where a number of aftershocks, according to the CSEM database have occurred (yellow circles in Figure 4). The resulting total seismic moment (2.4×10^{19} Nm) agrees with a M_W 6.9 earthquake.

4.2. Gentle SSW-Dipping Fault Scenario

In this case, the best-fitting uniform-slip solution is described by a 106° WNW-ESE striking and 22° SSW-dipping transpressive (rake about 125°) fault (18 × 22 km) plane, in good agreement with the other and gentle dipping plane of the focal mechanisms (strike/dip/rake 110°/21°/126°) (U.S. Geological Survey, 2023). The average uniform slip is 1.2 m, which using a value of 30 GPa for rigidity, yields an estimated seismic moment of 1.7×10^{19} Nm, equivalent to a M_W 6.8 earthquake. The fault top of this model is quite consistent with one of the fault segments of the NAF (Figure 4b). The best-fitting slip distribution on the extended fault plane (50 × 80 km) is shown in Figure 4b. Also, in this case, the data are well reproduced (Figure 3) but the fit to the data does not improve significantly passing from the uniform-slip model to a variable slip model (Table S2 in Supporting Information S1). The coseismic slip distribution shows a major asperity with peak slip of about 2.2 m down-dip respect to the hypocenter, thus leaving the upper portion of the modeled fault unbroken, where numerous aftershocks, according to the IPMA database have occurred (magenta circles in Figure 4). The resulting total seismic moment (2.3×10^{19} Nm) agrees with a M_W 6.8 earthquake.

4.3. Static Coulomb Stress Change

Coseismic slip induces changes in static stress that may trigger subsequent earthquakes as well as aseismic slip episodes on nearby faults and/or on unbroken parts of the causative fault itself (e.g., Cheloni et al., 2016; Lin & Stein, 2004). To investigate these variations, we calculated the static Coulomb stress changes induced by the 8 September 2023, M_W 6.8, mainshock using both our two preferred slip distributions on faults segments with the same mechanism as the main event, assuming an effective friction of 0.4, as is commonly used in stress interaction studies (e.g., Akinci & Antonioli, 2013; Freed, 2005).

As expected, the stress on the portions of the fault that slipped during the earthquake is lower, with increasing stress on the borders and of the upper parts of the modeled faults (Figure 5), where numerous aftershocks (that

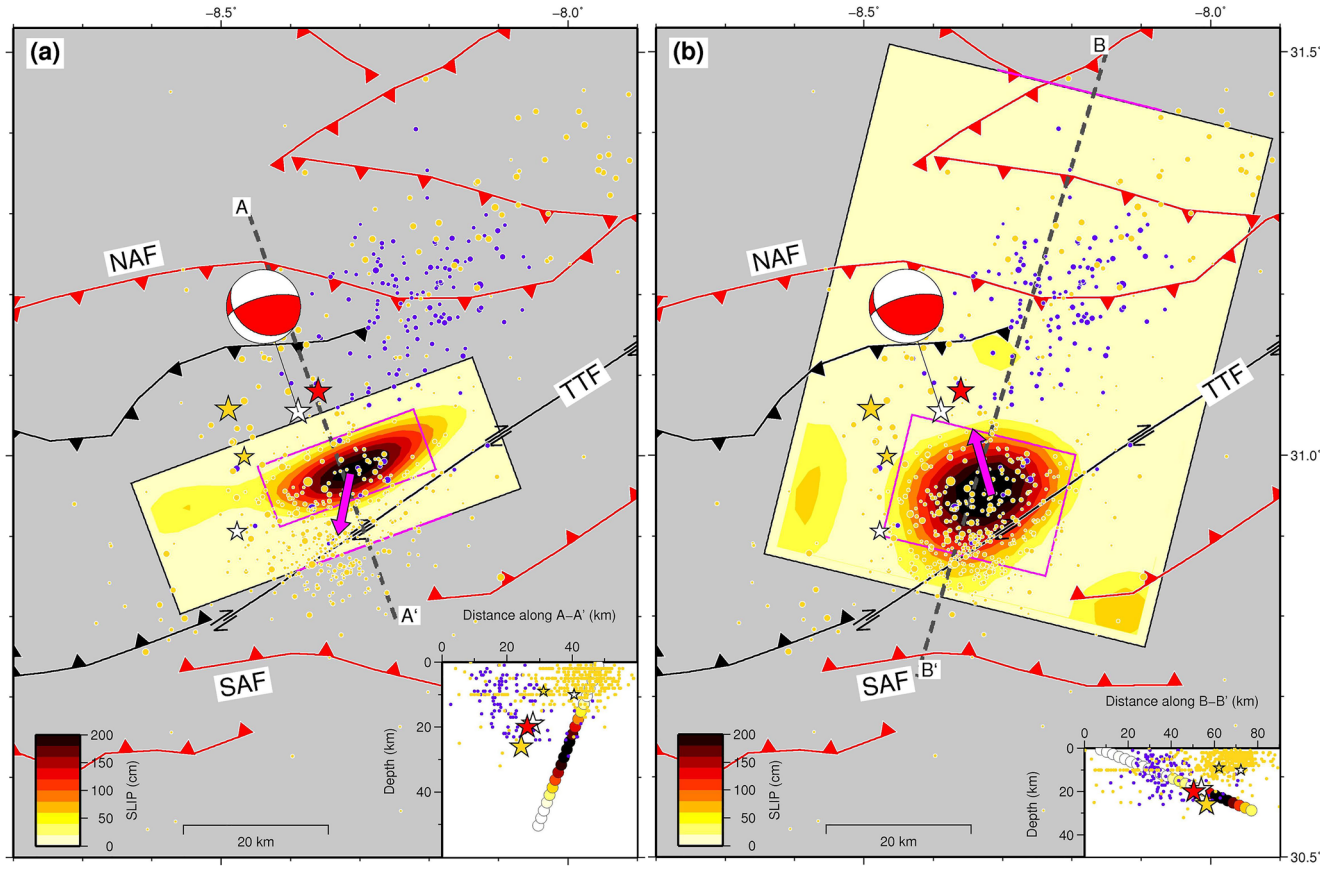

Figure 4. Geodetic models of the 8 September 2023, M_W 6.8, Morocco earthquake. (a) High-angle NNW-dipping fault and (b) gentle-angle SSW-dipping fault scenario, respectively, obtained by inverting interferometric synthetic aperture radar data. Solid lines are the major faults of the area (modified from Sebrier et al. (2006)). Magenta (Institute for Sea and Atmosphere) and yellow (Centre Sismologique Euro-Méditerranéen [CSEM]) circles are aftershocks between 8 September and 12 October 2023. The stars represent the M_W 6.8 mainshock and the largest aftershock (M 4.9) of the sequence as located by different agencies (color symbols as in Figure 1). The violet box represents our best-fit uniform-slip solution. The violet arrow indicates the estimated slip vector. The inset shows a cross section drawn perpendicular to the strike of the modeled fault, showing the amount of slip at depth and the major events (stars) and aftershock (dots) locations, respectively. Abbreviations: NAF North Atlas Fault; SAF South Atlas Fault; and TTF Tizi n'Test Fault. Note that many hypocenters were located at a fixed depth of 10 km from the CSEM location.

are almost entirely shallower than the mainshock) occurred following the 8 September earthquake. In particular, if we consider the IPMA database (magenta dots in Figure 5), aftershocks are located mainly NNE of the mainshock epicenter, in a crustal volume loaded by our high-angle fault solution (Figure 5a), where, in the case of the gentle-angle fault model, this area represents the upper portion of the modeled SSW-dipping fault (Figure 5b). The CSEM aftershocks (yellow dots in Figure 5), located mainly S of the mainshock, coincide with the upper parts of our modeled high-angle NNW-dipping fault (Figure 5a) or with a crustal volume where in the low-angle solution we observed increased Coulomb stress (Figure 5b).

5. Discussion and Conclusions

The 8 September 2023, M_W 6.8, earthquake represents the largest seismic event affecting the Atlas Mountains that has been recorded with modern geodetic measurements. InSAR data show that the mainshock may have occurred either on a high-angle (70°) NNW-dipping fault associated with the TTF alignment, or on a low-angle (22°) SSW-dipping fault associated with a segment of the NAF, with slip only occurred on deeper parts of the fault (Figure 4). Although the distribution of the interferometric fringes (Figure S1 in Supporting Information S1) seems to suggest the high-angle solution, the two models fit the data equivalently (Figures 2 and 3 and Table S1 in Supporting Information S1), which is a common issue for earthquakes on blind faults. InSAR data and focal mechanisms enable therefore either possibility.

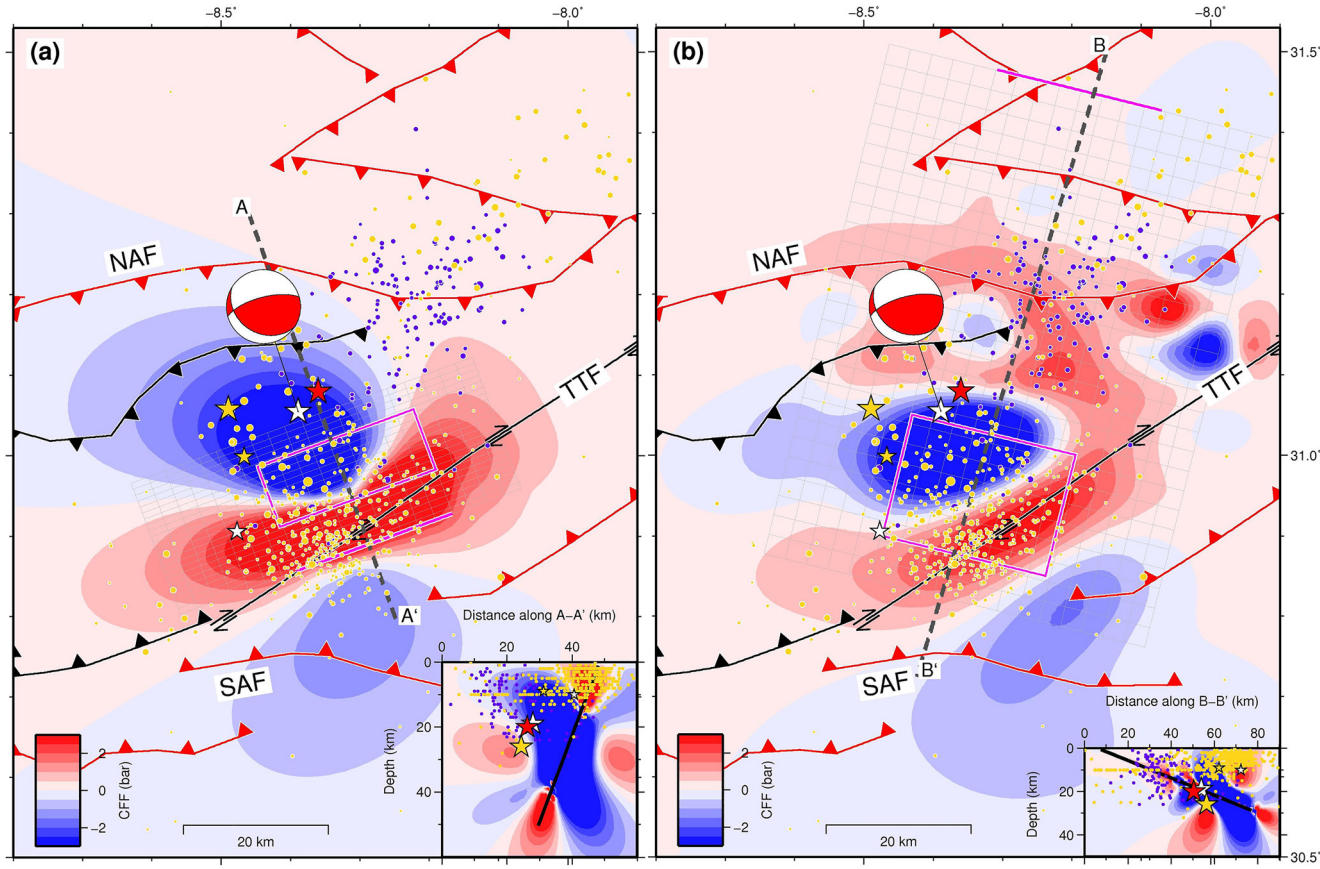

Figure 5. Coulomb stress changes produced by the 8 September 2023, M_W 6.8, Morocco earthquake. (a) High-angle NNW-dipping fault and (b) gentle-angle SSW-dipping fault scenario, respectively. The Coulomb stress changes are computed at a depth of 10 km. Coulomb stress profiles: perpendicular to the modeled fault, showing stress imparted by our preferred solution on transpressional NNW-dipping receiver faults (inset in panel (a)) and on SSW-dipping receiver faults (inset in panel (b)), together with aftershocks. Symbols as in Figure 4.

Even the available seismicity catalogs do not allow us to confidently identify the dip direction of the fault that slipped during the 2023 Morocco earthquake. In fact, the different seismic database shows different aftershock distributions with the CSEM catalog locating most earthquakes south of the main event (yellow circles in Figures 4 and 5), while the IPMA database locating them mainly north-northeast of the mainshock (magenta circles in Figures 4 and 5). The absence of a robust local seismic network might be a possible reason for this discrepancy. Our Coulomb stress analysis suggests that in both cases most of the aftershocks may have occurred in a crustal volume positively stressed due to stress redistribution following the 8 September earthquake (Figure 5).

Nevertheless, the following arguments could contribute to unraveling the seismotectonic issue and to constrain the real causative source. First, all the different locations (USGS, IPMA, and CSEM) of the 8 September 2023, M_W 6.8, earthquake do not match the steep NNW-dipping fault solution, being the hypocenters located more than 15 km to the north-northwest with respect to the fault plane (see inset of Figure 4a). In the case of the gentle SSW-dipping fault model there is instead a good correspondence between the positions of the mainshock hypocenter and our modeled fault (see inset of Figure 4b).

Second, gravity and heat flow data and modeling suggest a relatively thin crust (<40 km) as well as a regional scale mantle upwelling and lithosphere thinning (Teixell et al., 2005). As a consequence, based on rheological arguments the brittle-ductile transition, which represents a good proxy of the seismic-aseismic boundary (e.g., Maggini & Caputo, 2021) of the broader region is certainly much shallower than the Moho and hence most of the coseismic rupture surface associated with the high-angle NNE-dipping satellite-based fault model (Figure 4a) would be totally unrealistic.

A third possible constraint for selecting the proper fault model and resolving the seismological and satellite ambiguities is represented by geodynamic considerations, that is to say the Quaternary (Ait Brahim et al., 2002; Ellero

et al., 2012; Skikra et al., 2021) and present-day (Koulali et al., 2011; Sebrier et al., 2006) mean NW-SE horizontal direction of compression across the western High Atlas range. It is also worth to note that the crust (and the lithosphere) is largely affected by several major discontinuities inherited since the Paleozoic (Variscan orogenic phases), following the Mesozoic rifting and the initial Cenozoic inversion pulses. Accordingly, and combining the regional scale fabric (E-W to ENE-WSW trends) and the direction of compression, the western High Atlas is undergoing an oblique convergence resulting in a well-documented strain partitioning with high-angle to subvertical ENE-WSW trending dextral strike-slip faults (e.g., the Tizi n'Test Fault) and low- to intermediate-angle mainly reverse faults (North Atlas Fault and North Jebelet Fault). Once more, our NNW-dipping fault model (Figure 4a) should be neglected because with its reverse and left-lateral component of displacement it does not fit the above geometric and kinematic constraints. In contrast, the slip vector associated to the low-angle fault model (Figure 4b) is roughly perpendicular to the orogenic trend, therefore confirming that the causative fault has accommodated the purely contractional component in the frame of this oblique convergence.

As a final comment and as documented by the present work, we wish to stress the importance of integrating the interferometric analyses with other geological, tectonic, seismological, and geodetic data to unravel the ambiguities of satellite-based models.

Data Availability Statement

Seismicity used for this research is found online (IPMA database available at https://www.ipma.pt/en/geofisica/sismicidade; CSEM catalog, available at https://www.emsc-csem.org/). The down-sampled InSAR (Sentinel-1 and ALOS-2) data used for geodetic modeling in the study are provided online (https://doi.org/10.5281/zenodo.10403807).

Sentinel-1 data are copyright of Copernicus (2023). ALOS-2 PALSAR2 data are copyright of the Japan Aerospace Exploration Agency, JAXA (2023) and were obtained in the framework of the ER3A2N543 "Surface deformation analysis based on InSAR data."

Acknowledgments
We would like to thank the Editor, Dr Germán Prieto, and two anonymous reviewers for their constructive suggestions, which helped to improve the manuscript. All the figures were made using the GMT software (Wessel & Smith, 1998). Sentinel-1 data are copyright of Copernicus (2023). ALOS-2 PALSAR2 data are copyright of the Japan Aerospace Exploration Agency, JAXA (2023) and were obtained in the framework of the ER3A2N543 "Surface deformation analysis based on InSAR data."

References

Ait Brahim, L., Chotin, P., Hinaj, S., Abdelouafi, A., El Adraoui, A., Nakcha, C., et al. (2002). Paleostress evolution in the Moroccan African margin from triassic to present. *Tectonophysics*, *357*(1–4), 187–205. https://doi.org/10.1016/S0040-1951(2)00368-2

Akinci, A., & Antonioli, A. (2013). Observations and stochastic modeling of strong ground motions for the 2011 October 23 M_W 7.1 Van, Turkey, earthquake. *Geophysical Journal International*, *192*(3), 1217–1239. https://doi.org/10.1093/gji.ggs075

Atzori, S., Hunstad, I., Chini, M., Salvi, S., Tolomei, C., Bignami, C., et al. (2009). Finite fault inversion of DInSAR coseismic displacement of the 2009 L'Aquila earthquake (Central Italy). *Geophysical Research Letters*, *36*(15), L15305. https://doi.org/10.1029/2009GL039293

Bernard, D., Amrhar, M., Namous, M., Laville, E., Pedoja, K., & Dugué, O. (2011). Transpressional tectonics in the Marrakech high atlas: Insight by the geomorphic evolution of drainage basins. *Geomorphology*, *134*(3–4), 344–362. https://doi.org/10.1016/j.geomorph.2011.07.010

Bernard, D., Laville, E., Amhar, M., Namous, M., Dogue, O., & Pedoja, K. (2010). Quaternary evolution of the Marrakech high Atlas and morphotectonic evidence of activity along the Tizi N'Test Fault, Morocco. *Geomorphology*, *118*(3–4), 262–279. https://doi.org/10.1016/j.geomorph.2010.01.006

Calais, E., DeMets, C., & Nocquet, J.-M. (2003). Evidence for a post-3.16-Ma change in Nubia-Eurasia-North America plate motions? *Earth and Planetary Science Letters*, *216*(1–2), 81–92. https://doi.org/10.1016/S0012-821X(03)00482-5

Cheloni, D., & Akinci, A. (2020). Source modelling and strong ground motion simulations for the 24 January 2020, Mw 6.8 Elazig earthquake, Turkey. *Geophysical Journal International*, *223*(2), 1054–1068. https://doi.org/10.1093/gji/ggaa350

Cheloni, D., D'Agostino, N., D'Anastasio, E., Avallone, A., Mantenuto, S., Giuliani, R., et al. (2010). Coseismic and initial post-seismic slip of the 2009 Mw 6.3 L'Aquila earthquake, Italy, from GPS measurements. *Geophysical Journal International*, *181*, 1539–1546. https://doi.org/10.1111/j.1365-246X.2010.04584.x

Cheloni, D., Giuliani, R., D'Agostino, N., Mattone, M., Bonano, M., Fornaro, G., et al. (2016). New insights into fault activation and stress transfer between en echelon thrusts: The 2012 Emilia, Northern Italy, earthquake sequence. *Journal of Geophysical Research: Solid Earth*, *121*(6), 4742–4766. https://doi.org/10.1002/2016JB012823

Cherkaoui, T.-E., Medina, F., & Mridekh, A. (2017). Re-examination of the historical 11 May, 1624 Fez earthquake parameters. *Física de la Tierra*, *29*(0), 135–157. https://doi.org/10.5209/FITE.57469

Corana, A., Marchesi, M., Martini, C., & Ridella, S. (1987). Minimizing multimodal functions of continuous variables with the "Simulated Annealing" algorithm. *ACM Transactions on Mathematical Software*, *13*(3), 262–280. https://doi.org/10.1145/29380.29864

Costantini, M. (1998). A novel phase unwrapping method based on network programming. In *Geoscience and remote sensing, IEEE transactions on, may 1998* (Vol. 36, No. (3), pp. 813–821). https://doi.org/10.1109/36.673674

Ellero, A., Ottria, G., Malusà, M. G., & Ouanaimi, O. (2012). Structural geological analysis of the high Atlas (Morocco): Evidences of a transpressional fold-thrust belt. *Tectonics*. https://doi.org/10.5772/50071

Fialko, Y., Simons, M., & Agnew, D. (2001). The complete (3-D) surface displacement in the epicentral area of the 1999 Mw 7.1 Hector Mine earthquake, California, from space geodetic observations. *Geophysical Research Letters*, *28*(16), 3063–3066. https://doi.org/10.1029/2001GL013174

Freed, T. G. (2005). Earthquake triggering by static, dynamic, and post-seismic stress transfer. *Annual Review of Earth and Planetary Sciences*, *33*(1), 335–367. https://doi.org/10.1146/annurev.earth.33.092203.122505

Goldstein, R. M., & Werner, C. L. (1998). Radar interferogram filtering for geophysical applications. *Geophysical Research Letters*, *25*(21), 4035–4038. https://doi.org/10.1029/1998GL900033

Grunthal, G., & Whalstrom, R. (2012). The European-Mediterranean Catalogue (EMEC) for the last millennium. *Journal of Seismology*, *16*(3), 535–557. https://doi.org/10.1007/s10950-012-9302-y

Koulali, A., Ouazar, D., Tahayt, A., King, R. W., Vernant, P., Reilinger, R. E., et al. (2011). New GPS constraints on active deformation along the Africa-Iberia plate boundary. *Earth and Planetary Science Letters*, *308*(1–2), 211–217. https://doi.org/10.1016/j.epsl.2011.05.048

Lin, J., & Stein, R. S. (2004). Stress triggering in thrust and subduction earthquakes, and stress interaction between the southern San Andreas and nearby thrust and strike-slip faults. *Journal of Geophysical Research*, *109*(B2), B02303. https://doi.org/10.1029/2003JB002607

Lohman, R. B., & Simons, M. (2005). Some thoughts on the use of InSAR data to constrain models of surface deformation: Noise structure and data downsampling. *Geochemistry, Geophysics, Geosystems*, *6*(1), Q01007. https://doi.org/10.1029/2004GC000841

Maggini, M., & Caputo, R. (2021). Seismological data *versus* rheological modelling: Comparison across the Aegean region for improving the seismic hazard assessment. *Journal of Structural Geology*, *145*, 104312. https://doi.org/10.1016/j.jsg.2021.104312

McClusky, S., Reilinger, R., Mahmoud, S., Ben Sari, D., & Tealeb, A. (2003). GPS constraints on Africa (Nubia) and Arabia plate motions. *Geophysical Journal International*, *155*(1), 126–138. https://doi.org/10.1046/j.1365-246X.2003.02023.x

Medina, F., & Cherkaoui, T. (1991). Focal mechanisms of the Atlas earthquakes and tectonic implications. *Geologische Rundschau*, *80*(3), 639–648. https://doi.org/10.1007/bf01803691

Nocquet, J. M. (2003). Present-day kinematics of the Mediterranean: A comprehensive overview of GPS results. *Tectonophysics*, *579*, 220–242. https://doi.org/10.1016/j.tecto.2012.03.037

Okada, Y. (1985). Surface deformation due to shear and tensile faults in a half-space. *Bulletin of the Seismological Society of America*, *75*(4), 1135–1154. https://doi.org/10.1785/BSSA0750041135

Ouayah, M., Namous, M., Ourrubane, M., Elaloui, A., Krimissa, S., Nacaur, H. A., & Ziadi, K. (2021). Assessment of relative tectonic activity using morphotectonic analysis in the Central High Atlas, Demnate region, Morocco. *Arabian Journal of Geosciences*, *14*(813), 813. https://doi.org/10.1007/s.12517-021-07126-y

Rovida, A., & Antonucci, A. (2021). EPICA - European PreInstrumental earthquake CAtalogue, version 1.1 [Dataset]. Istituto Nazionale di Geofisica e Vulcanologia (INGV). https://doi.org/10.13127/epica.1.1

Sebrier, M., Siame, L., Zouine, E. M., Winter, T., Missenard, Y., & Leturmy, P. (2006). Active tectonics in the Moroccan high Atlas. *Geoscience*, *338*(1–2), 65–79. https://doi.org/10.1016/j.crte.2005.12.001

Serpelloni, E., Vannucci, G., Pondrelli, S., Argnani, A., Casula, G., Anzidei, M., et al. (2007). Kinematics of the Western Africa-Eurasia plate boundary from focal mechanisms and GPS data. *Geophysical Journal International*, *169*(3), 1180–1200. https://doi.org/10.1111/j.1365-246X.2007.03367.x

Skikra, H., Amrouch, K., Soulaimani, A., Lepretre, R., Ouabid, M., & Bodinier, J.-L. (2021). The intracontinental high Atlas belt: Geological overview and pending questions. *Arabian Journal of Geosciences*, *14*(12), 1071. https://doi.org/10.1007/s12517-021-07346-2

Takaku, J., Tadono, T., & Tsutsui, K. (2014). Generation of high resolution global DSM from ALOS PRISM., the international archives of the photogrammetry. In *Remote sensing and spatial information sciences* (Vol. XL-4, pp. 243–248). ISPRS.

Teixell, A., Ayarza, P., Zeyen, H., Fernàndez, M., & Arboleya, M.-L. (2005). Effects of mantle upwelling in a compressional setting: The Atlas mountains of Morocco. *Terra Nova*, *17*(5), 456–461. https://doi.org/10.1111/j.1365-3121.2005.00633.x

U.S. Geological Survey. (2023). Earthquake hazards program. Retrieved from http://earthquake.usgs.gov/earthquakes/map

Wessel, P., & Smith, W. H. F. (1998). New improved version of the generic mapping tools released. *Eos, Transactions American Geophysical Union*, *79*(47), 570. https://doi.org/10.1029/98EO00426